Heterogeneous & Homogeneous & Bio-

CHEMCATCHEM

CATALYSIS

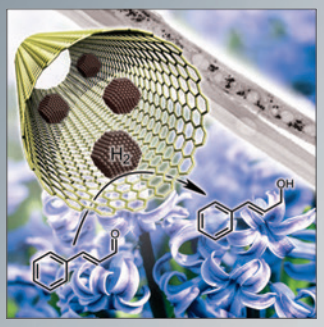

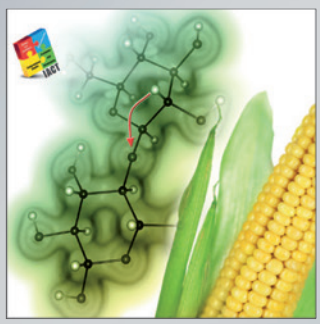

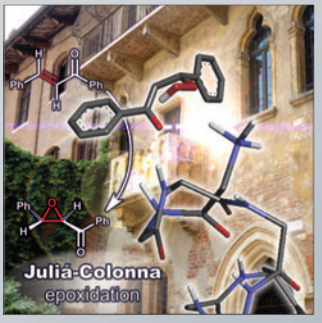

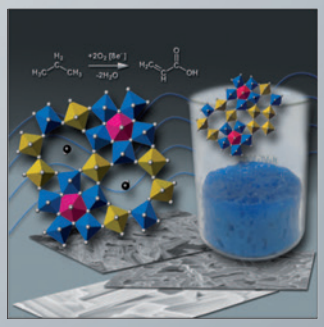

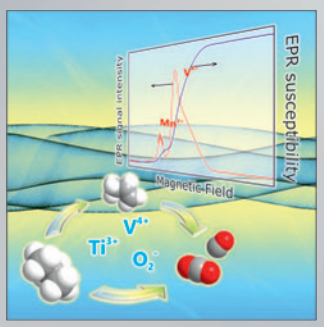

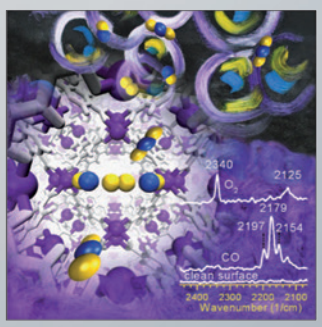

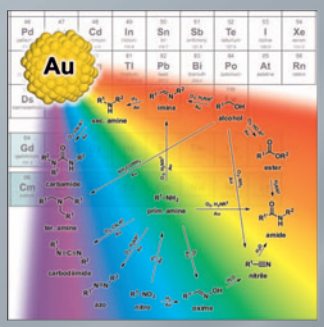

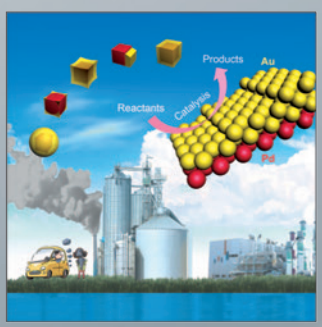

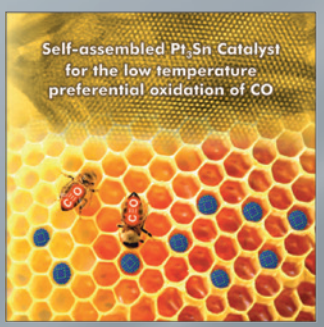

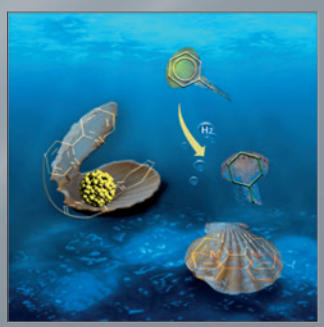

Reprint

A Journal of

ChemPubSoc Europe

WILEY-VCH

www.chemcatchem.org

ChemPubSoc Europe

DOI: 10.1002/cctc.201901084

CHEMCATCHEM Full Papers

Facile Synthesis of Fe/N/S-Doped Carbon Tubes as High-Performance Cathode and Anode for Microbial Fuel Cells

Wei Yang,*[a] Jun Li,*[b] Linghan Lan,[b] Zhuo Li,[b] Wenli Wei,[c, d] Jia En Lu,[c] and Shaowei Chen*[c]

As a renewable energy technology, microbial fuel cell (MFC) has been attracting increasing attention in recent decades. However, practical applications of MFCs has been hampered by the unsatisfactory electrode performance, in particular, at the cathode. Herein, Fe/N/S-doped carbon hollow tubes were prepared by a facile two-stage procedure involving hydrothermal treatment and pyrolysis at controlled temperatures. Electrochemical studies showed that the obtained samples exhibited an apparent electrocatalytic activity towards oxygen reduction reaction in both alkaline and acidic media, a performance comparable to that of commercial Pt/C, and the sample prepared at 800 °C stood out as the best among the series with a half-wave potential of +0.81 V vs. RHE and an electron transfer number of 3.98 at +0.6 V vs. RHE. The Fe/N/S-doped carbon tubes also exhibited a remarkable performance as an MFC anode by facilitating bacterial growth and electron transfer between the biofilm and electrode. In fact, an MFC based on the carbon tubes as both cathode and anode showed a markedly higher performance (maximum power density 479 W m^{-3}) than the control MFC based on a graphene aerogel anode and Pt/C cathode (359 W m^{-3}). These results suggest that Fe/N/S-doped carbon composites can be used for the fabrication of high-efficiency MFC electrodes.

Introduction

Microbial fuel cell (MFC) represents an energy conversion technology that uses anode microbes to catalyze the oxidation of organic substrates for electricity generation, and achieves power production and wastewater treatment simultaneously.[1] Of these, because of the simple structure and air breathing design, air cathode MFC has been attracting extensive attention in recent years.[2] In fact, significant progress in material synthesis, electrode design and operation parameter optimization has been achieved and contributed to a noticeable improvement in the performance of air cathode MFC.[3] However, the power output of MFCs remains unsatisfactory with regards to the need of practical applications. The performance of an air cathode MFC has been found to depend on a range of factors, such as the electron-transfer rate from bacteria to anode surface, kinetics of oxygen reduction reaction (ORR) at the cathode, ion diffusion/migration between anode and cathode, substrate supply in biofilm, and ion diffusion in cathode catalyst layer.[4] Among these, the construction of anode and cathode stands out as the most important factor influencing the MFC performance. In particular, the sluggish ORR kinetics at the cathode has been recognized as a primary bottleneck that limits the MFC performance.[5] Platinum-based catalysts have been widely used to facilitate the ORR process, but their high cost, scarcity and low durability hinder their practical utilization.[6] Recently, carbon doped with select (transition) metal and nonmetal elements has demonstrated high ORR activity towards ORR, and can be exploited as viable alternatives to platinum.[7] Of these, ternary iron and nitrogen-doped carbon (Fe/N/C) is considered as one of the most attractive candidates for fuel cell application, due to their remarkable ORR activity in both acid and alkaline solutions,[8] where the catalytic active sites are generally believed to arise from the FeN_x moieties and nitrogen dopants in the carbon matrix.[9] In addition, it has been shown that sulfur doping of the Fe/N/C catalysts can further enhance the ORR activity, where the half-wave potential ($E_{1/2}$) can be increased by as much as 0.3 V.[10] Experimentally, S-doping of Fe/N/C catalysts is typically achieved by a sequential process which entails pyrolyzing nitrogen-containing precursors to facilitate N doping, followed by mechanical mixing of metal salts and sulfur precursors to incorporate metal and sulfur dopants.[11] This method is rather tedious and unfavorable for homogenous

[a] Dr. W. Yang
State Key Laboratory of Hydraulics and Mountain River Engineering
College of Water Resource & Hydropower
Sichuan University
Chengdu 610065 (P. R. China)
E-mail: wei_yang@scu.edu.cn
[b] Prof. J. Li, L. Lan, Z. Li
Institute of Engineering Thermophysics
School of Energy and Power Engineering
Chongqing University
Chongqing 400030 (P. R. China)
E-mail: lijun@cqu.edu.cn
[c] Dr. W. Wei, Dr. J. E. Lu, Prof. Dr. S. Chen
Department of Chemistry and Biochemistry
University of California
Santa Cruz CA-95064 (USA)
E-mail: shaowei@ucsc.edu
[d] Dr. W. Wei
College of Chemistry and Chemical Engineering
Lanzhou University
Lanzhou 730000 (P. R. China)

Supporting information for this article is available on the WWW under https://doi.org/10.1002/cctc.201901084

This manuscript is part of the Special Issue "Electrocatalysis: From Batteries to Clean Energy Conversion", which is part of the wider project "Building A New Energy Economy with Catalysis".

dispersion of the active sites.[12] A facile approach is desired for the preparation of S-doped Fe/N/C.

On the anode, it has been found that the dissimilatory metal-reducing bacteria *Geobacter* species and *Shewanella oneidensis* can use Fe^{3+} as electron acceptors, and utilize the Fe 3d electrons as a long-distance electron transfer conduit.[13] Interestingly, previous studies have shown that the *Geobacter* species grows apparently, concurrently with increasing Fe^{3+} reduction, suggesting that the introduction of Fe^{3+} may stimulate the bacteria growth on the anode surface.[14] In addition, it has been shown that elemental sulfur can mediate electron-shuttling during iron reduction by dissimilatory metal-reducing bacteria.[15] Therefore, one can expect that a S-doped Fe/N/C carbon anode may facilitate bacteria growth and electron transfer. Another factor affecting the anode performance is the space accommodation of bacteria growth, proton transport and substrate supply.[14b] Three-dimensional graphene aerogel (GA) with a hierarchical porous structure has been used extensively as an anode material, and substantial progress has been made in enhancing the efficiency of current generation.[16] However, the performance of GA alone remains unsatisfactory, due to the limited growth and cultivation of bacteria in the interior of the anode.

Herein, we prepared well-defined S-doped Fe/N/C carbon tubes as electrode materials for both MFC cathode and anode by using a one-pot synthesis method. The obtained nanocomposites showed an apparent ORR activity. In addition, the carbon tubes were used as a structural scaffold to fabricate a three-dimensional carbon tube/graphene oxide aerogel anode, where the abundant macropores were found to facilitate bacteria growth, electrolyte transport and electron transfer. An MFC using the obtained S-doped Fe/N/C as both cathode and anode achieved a power density that was markedly higher than that of a control based on a graphene aerogel anode and Pt/C cathode.

Results and Discussion

The preparation procedure of carbon tubes is schematically shown in Figure 1a. Specifically, methyl orange and $FeCl_3$ reacted and produced fibrillar complexes, which served as structural templates for pyrrole polymerization, and hollow nanotubular structures were formed due to the self-degradation of the fibrillar templates. In this process, the Fe species and methyl orange were adsorbed into the polypyrrole tubes, and controlled pyrolysis at elevated temperatures led to the incorporation of Fe, N and S into the carbon framework. SEM measurements showed that the obtained samples indeed exhibited a fibrillar structure with a diameter of 150–200 nm and length of 5–10 μm (Figure S1); and in both bright-field and dark-field TEM studies (Figure 1b–c), the samples can be seen to exhibit a hollow tubular structure. Notably, the morphology remained virtually unchanged before and after pyrolysis (Figure S2). From the high-resolution TEM image in Figure 1d, the carbon tubes can be seen to have a wall thickness of ~20 nm and an amorphous carbon structure, which was also evidenced

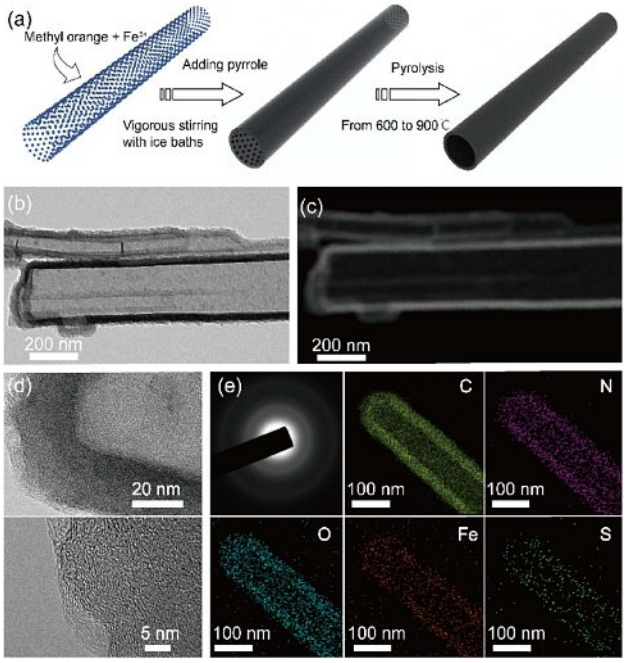

Figure 1. (a) Schematic illustration of the preparation procedure of carbon tubes. (b) Bright-field and (c) dark-field TEM images, (d) high resolution TEM images, (e) electron diffraction patterns and element mapping images of CT-800.

by the diffusive electron diffraction patterns (Figure 1e). In elemental mapping analysis, the elements of Fe, N, S, C and O can be seen to be distributed homogeneously within the carbon tubes (Figure 1e). In conjunction with the absence of any nanoparticle in the samples, this suggests that Fe was most likely atomically dispersed within the carbon matrix.

The structures of the carbon tube samples were further probed by XRD measurements. From Figure 2a, it can be seen that all samples display only two broad peaks at $2\theta = 24°$ and 44° that are consistent with the (002) and (101) diffractions of graphitic carbon; and the broad peaks suggest a low degree of crystallinity of the samples. For the pre-pyrolysis CT-pre sample, two major sharp diffraction peaks can be identified at 17.45° and 20.10°, most likely due to FeO_x formed by hydrolysis of $FeCl_3$.[17] However, these diffraction features vanished after pyrolysis at elevated temperature, indicating the absence of metal/metal oxide nanoparticles in the samples, in good agreement with results from TEM measurements (Figure 1). In addition, it can be noticed that the carbon (002) diffraction peaks shifted from 23.9° to 24.5° from CT-600 to CT-900, implying a shrinking interlayer spacing, most likely due to an increasing loss of N, S and Fe dopants with the increase of pyrolysis temperature (*vide infra*); meanwhile, the carbon (101) diffraction peak became intensified, suggesting improved graphitization of the samples. The structural defects and graphitization of the carbon tubes were further evaluated by Raman measurements. All samples show a D band at 1343 cm^{-1} and a G band at 1580 cm^{-1}, and the intensity ratios (I_G/I_D) decreased with increasing pyrolysis temperatures at 4.74 for CT-

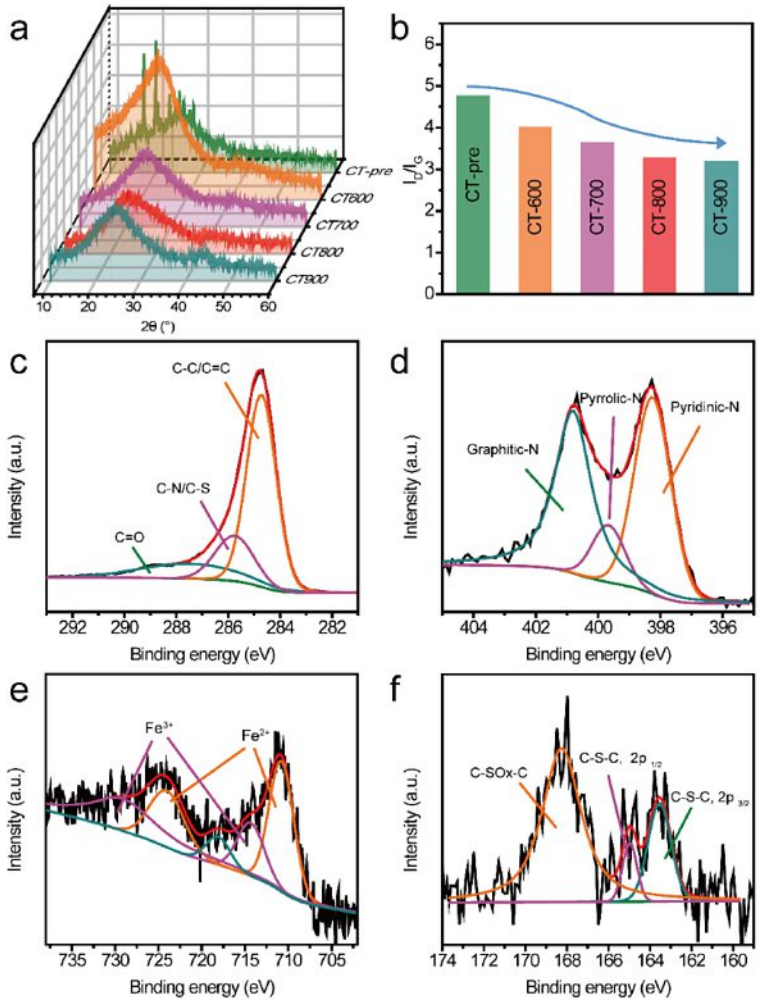

Figure 2. (a) XRD patterns and (b) I_G/I_D ratios of the carbon tube samples. High-resolution XPS scans of the (c) C 1s, (d) N 1s, (e) Fe 2p and (f) S 2p electrons of CT-800.

pre, 3.99 for CT-600, 3.62 for CT-700, 3.26 for CT-800 and 3.18 for CT-900 (Figure 2b and S3), suggesting that increasing the pyrolysis temperature effectively improved the degree of graphitization of the carbon tubes, in good agreement with results from XRD analysis.

The elemental compositions and valence state of the samples were then analyzed by XPS measurements. From the XPS full spectra (Figure S4), the C 1s, N 1s, S 2p and Fe 2p electrons can be clearly identified at 286, 400, 166 and 720 eV, respectively, for all samples in the series, indicating that N, S and Fe were indeed doped into the carbon framework. Based on the integrated peak areas, carbon was found to account for over 80 at.%, and the N content decreased somewhat from 13.40 at.% for CT-600 to 9.17 at.% for CT-700, 10.58 at.% for CT-800 and 5.97 at.% for CT-900 (Table S1). The high-resolution scans for the C 1s electrons of the sample are depicted in Figure 2c and S5a. Deconvolution yields three subpeaks at 284.7, 285.7 and 288.6 eV, which can be assigned to C–C/C=C, C–N/C–S, and C=O, respectively.[10] The high-resolution N 1s spectra can also be deconvoluted into three components, pyridinic-N/FeN_x (398.2 eV), pyrrolic-N (399.4 eV) and graphitic-N (400.9 eV) (Figure 2d and S5b).[18] Interestingly, the pyrrolic-N content diminished markedly from 9.08 at.% for CT-pre to 4.06 at.% for CT-600, 0.99 at.% for CT-700, 0.46 at.% for CT-800, and only 0.24 at.% for CT-900, due to its thermal instability.[19] In addition, it can be found that CT-800 displayed the highest graphitic-N content of 7.06 at.% among the series of samples (Table S1 and Figure S6). In the Fe 2p spectra, two pairs of peaks can be resolved at 710.4/723.4 eV and 714.3/729 eV, corresponding to the 2p electrons of Fe^{2+} and Fe^{3+}, respectively.[19] Note that the former is consistent with Fe^{2+} in FeN_x moieties;[18b] and no metallic Fe was seen in the spectra, indicating the absence of Fe nanoparticles in the carbon tubes (Figure 2e and S5c). For the S 2p spectra (Figure 2f and S5d), three subpeaks, 163.8 and 164.8 eV for the $2p_{3/2}$ and $2p_{1/2}$ electrons of C–S–C species, and 168.0 eV for oxidized sulfur (C–SO_x–C), indicating the successful doping of S into the carbon skeletons. The C–S–C species have been previously identified as catalytically active site towards ORR.[20]

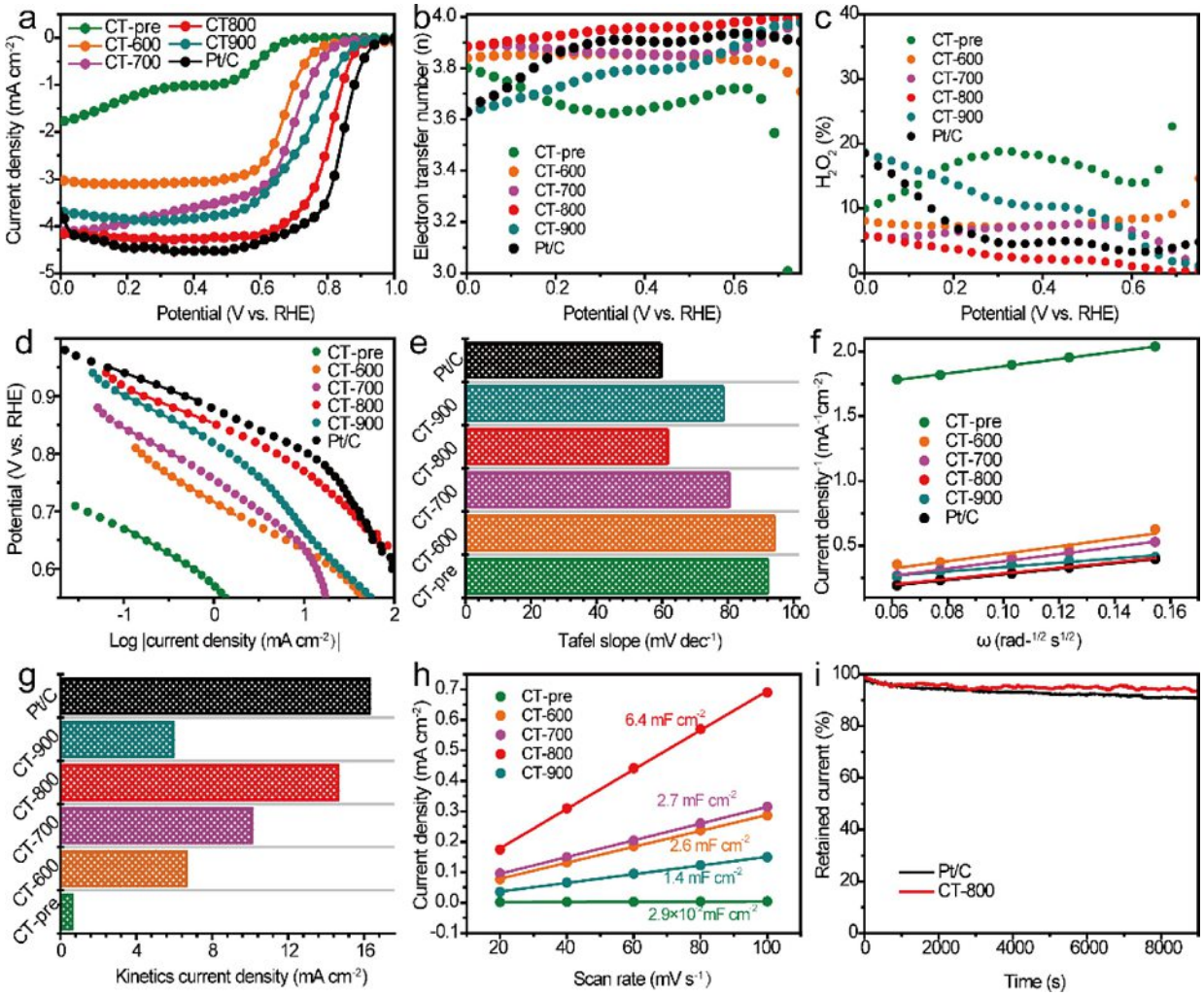

Figure 3. (a) LSV curves, (b) electron transfer number, (c) H_2O_2 yield, (d) Tafel curves, (e) Tafel slopes based on fitting results, (f) Koutecky-Levich plots at +0.6 V, (g) kinetic current densities at +0.6 V, and (h) double layer capacity of sample CT-pre, CT-600, CT-700, CT-800, CT-900 and Pt/C, (i) chronoamperometric profiles of CT-800 and Pt/C at the potential of +0.7 V vs. RHE in 0.1 M KOH.

The ORR performance of the samples was then evaluated by RRDE measurements in 0.1 M KOH. From Figure S7, one can see that the carbon tubes all exhibited an apparent ORR activity. The electrocatalytic activity of the samples was then compared at the rotating rate of 1600 rpm (Figure 3a), where the $E_{1/2}$ of CT-pre, CT-600, CT-700, CT-800, and CT-900 can be estimated to be +0.52, +0.68, +0.69, +0.81, and +0.75 V, with the limiting current density of 1.79, 3.11, 4.15, 4.26, and 3.89 mA cm^{-2}, respectively. One can see that CT-800 stood out as the best among the series, with a performance highly comparable to that of Pt/C (+0.84 V, 4.52 mA cm^{-2}). Previous studies have demonstrated that the ORR activity is correlated with the heteroatom doping in the carbon framework, in which the graphitic-N, pyridinic-N, graphitic-N, S and Fe dopants all contributed to the ORR activity.[20–21] In the present study (Table S1), CT-800 exhibited the highest graphitic-N content (7.06 at%) among the series, but only a rather comparable content of pyridinic-N/FeN_x, and C–S–C species, suggesting that graphitic-N was the dominant catalytic active site for ORR.[19] However, it should be pointed out that although CT-pre has the highest Fe, pyridinic-N, and S contents, it shows only a rather poor ORR performance. This is likely due to the high structural defects and low degree of graphitization, as manifested in Raman and XRD measurements (Figure 2 and S3).

To further investigate the ORR performance, the electron transfer numbers (n) were evaluated by Equation (1)

$$n = \frac{4i_{disk}}{i_{disk} + i_{ring}/N_r} \quad (1)$$

where i_{disk} is the disk current of oxygen reduction, i_{ring} is the ring current of hydrogen peroxide oxidation, and N_r is the collection efficiency of the gold ring (0.4). One can see that all samples exhibited n values higher than 3.6, for example, at +0.6 V, n = 3.72 for CT-pre, 3.83 for CT-600, 3.87 for CT-700, 3.98 for CT-800, and 3.89 for CT-900, in comparison to 3.93 for Pt/C (Figure 3b); the corresponding H_2O_2 yield was evaluated by Equation (2)

$$H_2O_2\% = \frac{200 i_{ring}}{i_{ring} + i_{disk}/N_r} \quad (2)$$

which was 14.11% for CT-pre, 8.34% for CT-600, 6.58% for CT-700, 1.16% for CT-800, 5.73% for CT-900 and 3.29% for Pt/C (Figure 3c). Again, one can see that CT-800 outperformed others in the series and even benchmark Pt/C. From the Tafel plots at 1600 rpm (Figure 3d), one can see that CT-800 displayed the lowest Tafel slope among the carbon tube series: 92 mV for CT-pre, 94 mV for CT-600, 81 mV for CT-700, 62 mV for CT-800, 79 mV for CT-900 and 60 mV for Pt/C (Figure 3e). Additionally, from the Koutecky-Levich plots at +0.6 V (Figure 3f), CT-800 exhibited the highest kinetics current density in the series: 0.62 mA cm^{-2} for CT-pre, 6.63 mA cm^{-2} for CT-600, 10.10 mA cm^{-2} for CT-700, 14.63 mA cm^{-2} for CT-800, 5.95 mA cm^{-2} for CT-900, and 16.29 mA cm^{-2} for Pt/C (Figure 3g).

The high ORR performance of CT-800 can be correlated to the electrochemical surface area (ECSA), which was quantified by the electrode double-layer capacitance (C_{dl}).[22] The cyclic voltammograms of the carbon tube samples were acquired at the potential sweep rate of 20 to 100 mV s^{-1} within the potential range of +1.1 to +1.2 V vs. RHE, where no faradaic current was produced (Figure S8). The C_{dl} was estimated to be 2.9×10^{-2} mF cm^{-2} for CT-pre, 2.6 mF cm^{-2} for CT-600, 2.7 mF cm^{-2} for CT-700, 6.4 mF cm^{-2} for CT-700 and 1.4 mF cm^{-2} for CT-900 (Figure 3h). One can see that there is a clear correlation between the ECSA and ORR activity.

The stability of the CT-800 sample was then evaluated by chronoamperometric (CA) and LSV tests. As shown in Figure 3i, the current responses of both CT-800 and Pt/C showed a slight decrease after 9000 s' continuous operation, but 93% of the current was retained for CT-800, slightly higher than that (90%) for Pt/C. The LSV tests of CT-800 also showed only a 15 mV cathodic shift in $E_{1/2}$ after 5,000 cycles (Figure S9), suggesting high stability of the CT-800 sample.

The ORR activity of the as-prepared carbon tubes was also evaluated in acidic media. LSV measurements in 0.5 M H_2SO_4 at 1600 rpm showed that the CT-pre, CT-600, CT-700, CT-800, CT-900 and Pt/C samples exhibited an $E_{1/2}$ of +0.34, +0.36, +0.66, +0.51 and +0.80 V, and the limiting current density of 3.78, 4.28, 4.73, 3.74 and 4.16 mA cm^{-2}, respectively (Figure S10a). Although the performance of CT-800 is lower than that of Pt/C, it is still attractive, as compared to those of non-precious metal catalysts. As depicted in Figure S10b, all samples exhibited n values higher than 3.5 in the potential range of 0 to +0.6 V, with the highest observed with CT-800 and Pt/C (n = 3.95 and 3.94, respectively), suggesting that CT-800 facilitated the ORR through a four-electron pathway even in acidic media. In addition, it can be found that CT-800 and Pt/C show a low H_2O_2 yield of 2.49% and 3.15%, respectively. Taken together, these results confirmed that the CT-800 sample indeed can be used as a viable catalyst towards ORR.

Apart from the remarkable ORR catalytic activity, the CT-800 sample was also found to facilitate the electron transfer and growth of dissimilatory metal-reducing bacteria on the electrode surface, due to its Fe and S dopants (e.g., Fe^{3+} can serve as an electron acceptor).[4a,13a,14a,15] Therefore, CT-800 is a promising material for MFC anode as well. Experimentally, a CT-800/GA hybrid anode was prepared by taking advantage of the abundant pore structure, excellent biocompatibility and electric conductivity of GA. After inoculation for one week, we cut the CT-800/GA sample and evaluated the biocompatibility and pore structure, in comparison to GA alone. From Figure 4a and S11, one can see that the bacteria cells were much more densely adhered onto the CT-800/GA electrode surface than on GA alone, revealing that the open macropore structure indeed enhanced the substrate supply and product removal and facilitated the growth of biofilm. These results suggested that the CT-800/GA indeed markedly improved the adhesion and growth of biofilm.

To further examine the electrode performance, the cyclic voltammograms of the bioanode were acquired under the turnover condition. It can be seen that the CT-800/GA bioanode displayed a maximum oxidation current density of 4536 A m^{-3}, which is significantly higher than that (2065 A m^{-3}) for GA alone (Figure 4b). This is likely due to the higher biofilm catalytic activity which promoted electron transfer between the anode surface and biofilm. Electrochemical impedance measurements were then performed to examine bacteria adhesion on the bioanode. The Nyquist plots are shown in Figure 4c, which were fitted by the EClab 11.10 program according to the equivalent circuit in Figure 4c inset, and the results were listed in Table S2. It can be found that the charge transfer resistance (R_{ct}) of CT-800/GA bioanode is only 264.1 Ω, much lower than 316.8 Ω for GA bioanode, confirming faster electron-transfer kinetics of CT-800/GA. Apart from the anode, the performance of the CT-800 and Pt/C cathodes was also evaluated and compared by LSV measurements. One can see that the CT-800 and Pt/C air cathodes showed similar current responses in the potential range of −0.1 to +0.1 V vs. Ag/AgCl, indicating a comparable cathode performance. After inoculation, the power densities and polarization curves were acquired, as depicted in Figure 4e. It can be seen that the cell voltage of the CT-800/GA//CT-800 MFC decreased more slowly with the increase of current density, suggesting a better polarization performance and a lower internal resistance than the GA//Pt/C MFC. In addition, the former MFC delivered a maximum power density of 479 W m^{-3}, which is higher than that of the latter (359 W m^{-3}) (Figure 4e). Significantly, the anode and cathode polarization curves further revealed that the CT-800 cathode had a performance that was comparable to that of Pt/C, while the CT-800/GA anode achieved a much higher performance than GA alone (Figure 4f). These results collectively demonstrated the feasibility of the carbon tubes as effective electrode materials in the fabrication of both MFC anodes and cathodes.

Conclusions

In this study, Fe/N/S carbon hollow tubes were prepared by a two-stage method involving one-pot hydrothermal treatment and pyrolysis at controlled temperatures. Electrochemical

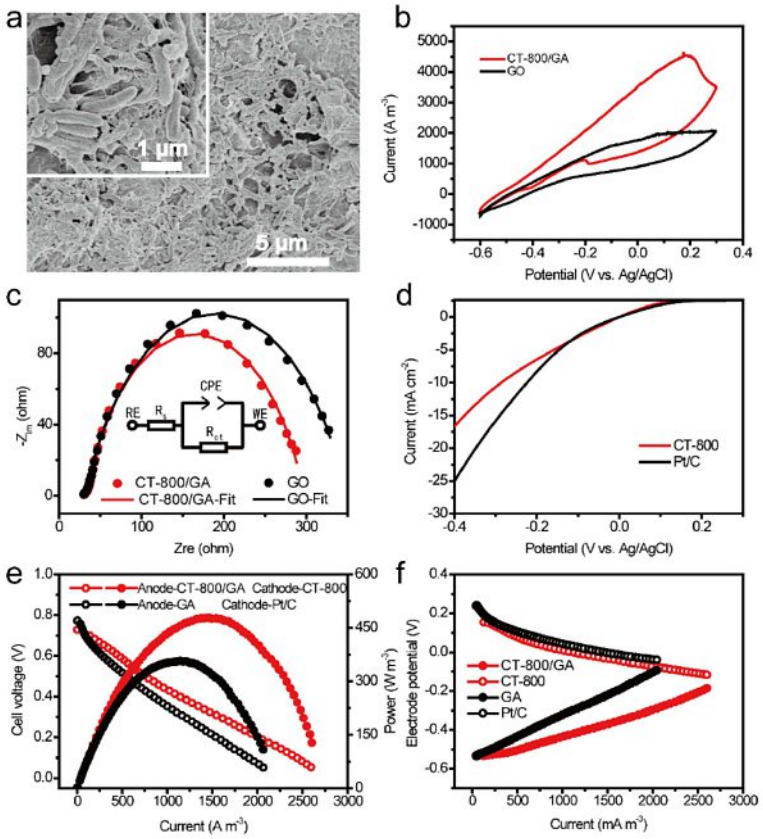

Figure 4. (a) SEM image of the surface of GO/CT composite anode, (b) cyclic voltammograms of biofilms on composite anode (red curve) and rGO anode (black curve), (c) Nyquist plots of composite anode (red curve) and rGO anode (black curve) (inset is the equivalent circuit, where R_s and R_{ct} represent the solution ohmic resistance and charge transfer resistance, respectively, and CPE represents the double layer capacitance), (d) LSV curves of air cathode using CT-800 (red curve) and Pt/C (black curve) catalysts, and (e) power density and polarization curves of MFCs, and cathode and anode potentials of CT/GA anode-CT-800 cathode (red dot) and rGO anode-Pt/C cathode (black dot).

studies showed that among the series towards, the samples prepared at 800 °C exhibited the best catalytic activity ORR in both alkaline and acid media, a performance comparable to that of commercial Pt/C. This was largely ascribed to the combined contributions of a high degree of graphitization and high graphitic-N content in the carbon framework. Interestingly, the carbon tubes were also found to facilitate bacteria adhesion and electron transfer between biofilm and electrode surface, and thus might be used as a high-performance anode material as well. An MFC based on the obtained carbon tubes as both anode and air cathode was found to achieve a markedly higher performance than the control MFC with a GA anode and commercial Pt/C cathode. These results suggest the high feasibility of as prepared carbon tubes for both anode and cathode fabrication in MFC applications.

Experimental Section

Preparation of Graphene Oxide and Carbon Tubes

Graphene oxide was prepared by using the modified Hummers method.[23] Briefly, graphitic powders (2 g, 99.8%, Alfa Aesar) were added into the mixture of H_2SO_4 (46 mL, 98%, Fisher Chemicals) and HNO_3 (10 mL, 65%, Fisher Chemicals) under vigorous stirring in an ice bath. Then, $KMnO_4$ was slowly added into the mixture and stirred for 1 h. The mixture was then diluted with Nanopure water (46 mL, Barnstead Nanopure water system, 18.3 MΩ cm) and stirred for another 2 h at 95 °C. When the suspension was cooled down to room temperature, additional Nanopure water (200 mL) and H_2O_2 (10 mL, 30%, Fisher Chemicals) was added. Finally, the precipitates were collected by centrifugation and washed with HCl (5 wt.%) for at least 5 times, and further washed with Nanopure water until the supernatant pH reached ca. 7.

Carbon tubes were prepared by using a self-template approach. In brief, 343.7 mg of methyl orange was dissolved in 220 mL of Nanopure water under magnetic stirring at room temperature, into which was then added 1703 mg of $FeCl_3 \cdot 6H_2O$. Then, 5 mL of ethanol containing 730 μL of pyrrole was slowly added into the solution in an ice bath, and the solution was stirred for 24 h at room temperature, producing a black flocculent precipitate (CT-pre). The precipitate was collected via centrifugation at 4500 rpm, washed with ethanol for at least 3 times, dried at 80 °C, and pyrolyzed at 600, 700, 800 and 900 °C, affording Fe/N/S carbon tubes that were denoted as CT-600, CT-700, CT-800 and CT-900, respectively.

Materials Characterization

The morphology of the carbon tubes was characterized with a scanning electron microscope (SEM, Hitachi S4800 P) and transmission electron microscope (TEM, 200 kV, JEM-2100F). Elemental mapping analysis was conducted using an EDX detector attached to the JEM-2100F scope. X-ray diffraction (XRD) patterns were acquired with a Bruker D8 Advance powder X-ray diffractometer equipped with Cu-K_α radiation at the scan rate of 5 min^{-1} from $2\theta =$ 5° to 90°. Raman spectra was collected on a Renishaw inVia system using a helium-neon gas laser (632.8 nm). X-ray photoelectron spectroscopy (XPS) analysis was performed on a Thermo Escalab 250XI using Al K_α radiation (1486.6 eV).

Electrochemistry

Electrochemical measurements were performed on a CHI710 electrochemical station in a three-electrode system. A Ag/AgCl (1 M KCl) and a graphite rod were used as the reference and counter electrode, respectively, while a rotating ring-disk electrode (RRDE, glassy carbon disk and gold ring, with the respective surface area of 0.246 and 0.188 cm^2) was used as the working electrode. The Ag/AgCl reference electrode was calibrated against a reversible hydrogen electrode (RHE). All potentials in this study were referenced to this RHE except for MFC experiments. The catalyst ink was prepared by dispersing 5 mg of the as-prepared catalysts into 2 mL of a water/isopropanol (v:v 1:2) mixture along with the addition of 100 μL of a 20 wt.% Nafion solution. After sonication of the mixture for at least 30 min, 20 μL of the catalyst ink was dropcast onto the glassy carbon disk and dried at room temperature, corresponding to a catalyst loading of 0.203 mg cm^{-2}. The current density during RRDE tests was obtained by normalizing the current to the disk electrode surface area.

The RRDE tests were first conducted in nitrogen-saturated 0.1 M KOH to obtain the baseline current, then switched to an oxygen-saturated solution to evaluate the ORR activity. Prior to the ORR tests, the electrode was electrochemically activated by potential cycling within the potential range of +1.2 to 0 V at the scan rate of 100 mV s^{-1}, until steady voltammetric profiles were reached.[2] Linear sweep voltammetry (LSV) tests were carried out at the scan rate of 10 mV s^{-1} from +1.2 to 0 V at the rotation rates of 400 to 2500 rpm. The ORR current was calculated by subtracting the current obtained in nitrogen-saturated solution from that in oxygen-saturated solution.

Electrode Fabrication and MFC Set-Up

Air cathode was fabricated using carbon cloth (WOS 1002 PHYCHEMi Co. Ltd., China) as the electrode substrate. In a typical preparation, the carbon cloth was teflonized by brushing a layer of polytetrafluoroethylene (PTFE, 60 wt.% solution, Sigma Aldrich) on one side and heat-treated at 370 °C for 20 min. This coating procedure was repeated 4 times.[23] Then, the CT-800 or Pt/C catalyst ink prepared above was cast onto the other side of the teflonized carbon cloth and dried at 80 °C. The diameter of the air cathode was 3 cm (corresponding to a surface area of ca. 7 cm^2), and the catalyst loading was calculated to be 2.0 mg cm^{-2} for CT-800 and 0.5 mg cm^{-2} for Pt/C.

The anode was prepared via a hydrothermal process followed by freeze drying. In brief, 25 mg of CT-800 and 25 mg of graphene oxide prepared above were dispersed in 10 mL of Nanopure water under sonication for 3 h. The mixture was then loaded into a 25 mL Teflon-lined reactor and sealed in a steel autoclave. The reactor was heated in an oven at 180 °C for 12 h to obtain a carbon tube/graphene composite hydrogel, which was then converted to a carbon tube/graphene aerogel (CT-800/GA) by freeze-drying overnight. Graphene aerogel (GA) alone was prepared as the control anode by using the same procedure except that CT-800 were replaced by a same amount of graphene oxide. The volume of the aerogel was about 0.5 cm^3 (0.8 cm in diameter, and 1 cm in length).

MFCs were constructed by fixing the anode and cathode prepared above on two sides of a cubic reactor with a cylindrical chamber (diameter 3 cm, length 4 cm, volume 28 mL). The anode-cathode spacing was 3 cm and the reference-cathode spacing was 1 cm. The anode and cathode were connected to an external resistor or external load through a titanium wire. The MFCs were inoculated using the effluent from an MFC that was fed with acetate over 2 years. After the start-up, the MFCs were fed with fresh growth media composed of 2.04 g L^{-1} sodium acetate, 11.82 g L^{-1} Na_2HPO_4, 2.32 g L^{-1} KH_2PO_4, 0.1 g L^{-1} NH_4Cl, 0.5 g L^{-1} NaCl, 0.1 g L^{-1} $MgSO_4 \cdot 7H_2O$, 15 mg L^{-1} $CaCl_2 \cdot 2H_2O$ and 1.0 mL L^{-1} trace elements.[24] All MFCs were operated under the fed-batch mode at the constant temperature of 30 ± 1 °C with an external resistor of 1000 Ω. The power density was calculated by Equation (3)

$$P = UI/V_{anode} \quad (3)$$

where U is the cell voltage, I is the current and V_{anode} is the volume of the anode (ca. 0.5 cm^3).

Acknowledgements

This work was supported by the National Natural Science Funds for Outstanding Young Scholars (No. 51622602), and the National Science Foundation (CHE-1710408 and CBET-1848841). TEM and XPS work was carried out at the National Center for Electron Microscopy and Molecular Foundry, Lawrence Berkeley National Laboratory, which is supported by the US Department of Energy, as part of a user project. W.Y. and W.L.W. thank the China Scholarship Council for a research fellowship.

Conflict of Interest

The authors declare no conflict of interest.

Keywords: microbial fuel cell · carbon tube · Fe/N/S doping · oxygen reduction reaction · bioanode

[1] a) W. W. Li, H. Q. Yu, Z. He, *Energy Environ. Sci.* **2014**, *7*, 911–924; b) Y. Yang, T. Liu, Q. Liao, D. Ye, X. Zhu, J. Li, P. Zhang, Y. Peng, S. Chen, Y. Li, *J. Mater. Chem. A* **2016**, *4*, 15913–15919.
[2] W. Yang, Y. Peng, Y. D. Zhang, J. E. Lu, J. Li, S. W. Chen, *ACS Sustainable Chem. Eng.* **2019**, *7*, 3917–3924.
[3] a) B. E. Logan, M. J. Wallack, K. Y. Kim, W. H. He, Y. J. Feng, P. E. Saikaly, *Environ. Sci. Technol. Lett.* **2015**, *2*, 206–214; b) H. Yuan, Y. Hou, I. M. Abu-Reesh, J. Chen, Z. He, *Mater. Horiz.* **2016**, *3*, 382–401; c) B. Bian, D. Shi, X. B. Cai, M. J. Hu, Q. Q. Guo, C. H. Zhang, Q. Wang, A. X. Sun, J. Yang, *Nano Energy* **2018**, *44*, 174–180.
[4] a) R. Wang, M. Yan, H. Li, L. Zhang, B. Peng, J. Sun, D. Liu, S. Liu, *Adv. Mater.* **2018**, 1800618; b) M. Oliot, S. Galier, H. R. de Balmann, A. Bergel, *Appl. Energy* **2016**, *183*, 1682–1704; c) K. Y. Cheng, G. Ho, R. Cord-Ruwisch, *Environ. Sci. Technol.* **2008**, *42*, 3828–3834; d) S. You, X. Gong, W. Wang, D. Qi, X. Wang, X. Chen, N. Ren, *Adv. Energy Mater.* **2016**, *6*,

1501497; e) S. C. Popat, D. Ki, B. E. Rittmann, C. I. Torres, *ChemSusChem* **2012**, *5*, 1071–1079.
[5] Q. Wang, X. Zhang, R. Lv, X. Chen, B. Xue, P. Liang, X. Huang, *J. Mater. Chem. A* **2016**, *4*, 12387–12391.
[6] C. Santoro, A. Serov, L. Stariha, M. Kodali, J. Gordon, S. Babanova, O. Bretschger, K. Artyushkova, P. Atanassov, *Energy Environ. Sci.* **2016**, *9*, 2346–2353.
[7] a) S. Li, C. Cheng, A. Thomas, *Adv. Mater.* **2017**, *29*, 1602547; b) C. Z. Zhu, H. Li, S. F. Fu, D. Du, Y. H. Lin, *Chem. Soc. Rev.* **2016**, *45*, 517–531.
[8] a) C. Santoro, A. Serov, C. W. Narvaez Villarrubia, S. Stariha, S. Babanova, A. J. Schuler, K. Artyushkova, P. Atanassov, *ChemSusChem* **2015**, *8*, 828–834; b) B. Lu, T. J. Smart, D. Qin, J. E. Lu, N. Wang, L. Chen, Y. Peng, Y. Ping, S. Chen, *Chem. Mater.* **2017**, 5617–5628; c) A. Serov, K. Artyushkova, P. Atanassov, *Adv. Energy Mater.* **2014**, *4*, 1301735.
[9] a) H. Tang, Y. Zeng, Y. Zeng, R. Wang, S. Cai, C. Liao, H. Cai, X. Lu, P. Tsiakaras, *Appl. Catal. B* **2017**, *202*, 550–556; b) D. Guo, R. Shibuya, C. Akiba, S. Saji, T. Kondo, J. Nakamura, *Science* **2016**, *351*, 361–365; c) Y. J. Sa, D. J. Seo, J. Woo, J. T. Lim, J. Y. Cheon, S. Y. Yang, J. M. Lee, D. Kang, T. J. Shin, H. S. Shin, H. Y. Jeong, C. S. Kim, M. G. Kim, T. Y. Kim, S. H. Joo, *J. Am. Chem. Soc.* **2016**, *138*, 15046–15056.
[10] K. Hu, L. Tao, D. Liu, J. Huo, S. Y. Wang, *ACS Appl. Mater. Interfaces* **2016**, *8*, 19379–19385.
[11] a) Y. C. Wang, Y. J. Lai, L. Song, Z. Y. Zhou, J. G. Liu, Q. Wang, X. D. Yang, C. Chen, W. Shi, Y. P. Zheng, M. Rauf, S. G. Sun, *Angew. Chem. Int. Ed.* **2015**, *54*, 9907–9910; *Angew. Chem.* **2015**, *127*, 10045–10048; b) C. Chen, X. D. Yang, Z. Y. Zhou, Y. J. Lai, M. Rauf, Y. Wang, J. Pan, L. Zhuang, Q. Wang, Y. C. Wang, N. Tian, X. S. Zhang, S. G. Sun, *Chem. Commun.* **2015**, *51*, 17092–17095.
[12] Y. J. Wu, Y. C. Wang, R. X. Wang, P. F. Zhang, X. D. Yang, H. J. Yang, J. T. Li, Y. Zhou, Z. Y. Zhou, S. G. Sun, *ACS Appl. Mater. Interfaces* **2018**, *10*, 14602–14613.
[13] a) D. R. Lovley, *Microbial. Rev.* **1991**, *55*, 259–287; b) R. Nakamura, A. Okamoto, N. Tajima, G. J. Newton, F. Kai, T. Takashima, K. Hashimoto, *ChemBioChem* **2010**, *11*, 643–645; c) X. C. Jiang, J. S. Hu, A. M. Lieber, C. S. Jackan, J. C. Biffinger, L. A. Fitzgerald, B. R. Ringeisen, C. M. Lieber, *Nano Lett.* **2014**, *14*, 6737–6742.
[14] a) O. L. Snoeyenbos-West, K. P. Nevin, R. T. Anderson, D. R. Lovley, *Microbial. Ecol.* **2000**, *39*, 153–167; b) S. Zhao, Y. Li, H. Yin, Z. Liu, E. Luan, F. Zhao, Z. Tang, S. Liu, *Sci. Adv.* **2015**, *1*, e1500372.
[15] T. M. Flynn, E. J. O'Loughlin, B. Mishra, T. J. DiChristina, K. M. Kemner, *Science* **2014**, *344*, 1039–1042.
[16] a) Y. Yang, T. Liu, X. Zhu, F. Zhang, D. Ye, Q. Liao, Y. Li, *Adv. Sci.* **2016**, *3*, 1600097; b) J. J. Mao, J. Iocozzia, J. Y. Huang, K. Meng, Y. K. Lai, Z. Q. Lin, *Energy Environ. Sci.* **2018**, *11*, 772–799.
[17] a) J. Monnier, S. Reguer, E. Foy, D. Testemale, F. Mirambet, M. Saheb, P. Dillmann, I. Guillot, *Corros. Sci.* **2014**, *78*, 293–303; b) W. Wei, H. B. Cong, H. X. Xiong, *Colloid Polym. Sci.* **2018**, *296*, 1205–1212; c) B. B. Zhang, J. L. Song, G. Y. Yang, B. X. Han, *Chem. Sci.* **2014**, *5*, 4656–4660.
[18] a) Y. Wang, N. N. Guo, L. K. Zhu, Y. Pan, R. W. Wang, Z. T. Zhang, S. L. Qiu, *Chem. Commun.* **2018**, *54*, 12974–12977; b) P. Z. Chen, T. P. Zhou, L. L. Xing, K. Xu, Y. Tong, H. Xie, L. D. Zhang, W. S. Yan, W. S. Chu, C. Z. Wu, Y. Xie, *Angew. Chem. Int. Ed.* **2017**, *56*, 610–614; *Angew. Chem.* **2017**, *129*, 625–629.
[19] W. H. Niu, L. G. Li, X. J. Liu, N. Wang, J. Liu, W. J. Zhou, Z. H. Tang, S. W. Chen, *J. Am. Chem. Soc.* **2015**, *137*, 5555–5562.
[20] D. H. Kwak, S. B. Han, Y. W. Lee, H. S. Park, I. A. Choi, K. B. Ma, M. C. Kim, S. J. Kim, D. H. Kim, J. I. Sohn, K. W. Park, *Appl. Catal. B* **2017**, *203*, 889–898.
[21] a) H. J. Shen, E. Gracia-Espino, J. Y. Ma, K. T. Zang, J. Luo, L. Wang, S. S. Gao, X. Mamat, G. Z. Hu, T. Wagberg, S. J. Guo, *Angew. Chem. Int. Ed.* **2017**, *56*, 13800–13804; *Angew. Chem.* **2017**, *129*, 13988–13992; b) N. Wang, B. Z. Lu, L. G. Li, W. H. Niu, Z. H. Tang, X. W. Kang, S. W. Chen, *ACS Catal.* **2018**, *8*, 6827–6836; c) S. H. Ahn, X. W. Yu, A. Manthiram, *Adv. Mater.* **2017**, *29*.
[22] Y. Peng, B. Z. Lu, L. M. Chen, N. Wang, J. E. Lu, Y. Ping, S. W. Chen, *J. Mater. Chem. A* **2017**, *5*, 19499–19499.
[23] W. Yang, G. Chata, Y. Zhang, Y. Peng, L. J. En, N. Wang, R. Mercado, J. Li, S. Chen, *Nano Energy* **2019**, *57*, 811–819.
[24] W. Yang, J. Li, D. Ye, X. Zhu, Q. Liao, *Electrochim. Acta* **2017**, *224*, 585–592.

Manuscript received: June 18, 2019
Revised manuscript received: August 5, 2019
Accepted manuscript online: August 9, 2019
Version of record online: September 25, 2019